Università degli Studi Mediterranea di Reggio Calabria
Archivio Istituzionale dei prodotti della ricerca

Physical Insight Unveils New Imaging Capabilities of Orthogonality Sampling Method

This is the peer reviewd version of the followng article:

Original
Physical Insight Unveils New Imaging Capabilities of Orthogonality Sampling Method / Bevacqua, M.T., Isernia, T., Palmeri, R., Akinci, M.N., Crocco, L.. - In: IEEE TRANSACTIONS ON ANTENNAS AND PROPAGATION. - ISSN 0018-926X. - 68:5(2020), pp. 4014-4021. [10.1109/TAP.2019.2963229]

Availability:
This version is available at: https://hdl.handle.net/20.500.12318/56137 since: 2020-12-18T19:25:44Z

Published
DOI: http://doi.org/10.1109/TAP.2019.2963229
The final published version is available online at:http://ieeexplore.ieee.org/stamp/stamp.jsp?tp=&

Terms of use:
The terms and conditions for the reuse of this version of the manuscript are specified in the publishing policy. For all terms of use and more information see the publisher's website

Publisher copyright

This item was downloaded from IRIS Università Mediterranea di Reggio Calabria (https://iris.unirc.it/) When citing, please refer to the published version.

(Article begins on next page)

24 June 2026

Physical Insight Unveils New Imaging Capabilities of Orthogonality Sampling Method

Martina T. Bevacqua, *Member, IEEE*, Tommaso Isernia, *Senior Member, IEEE*, Roberta Palmeri, Mehemet N. Akıncı Jr., *Member, IEEE*, and Lorenzo Crocco, *Senior Member, IEEE*

***Abstract*—The orthogonality sampling method is a recently introduced qualitative inverse scattering approach for the estimation of the morphological properties of unknown targets. Both the simplicity of implementation and the applicability to various measurement configurations make this method very effective. In this paper, a general physical understanding of the method is given for the first time. Such an interpretation is derived from the relationship between the currents induced in the investigated scenario and the so-called *reduced* scattered field, which is the core of the orthogonality sampling indicator function. Interestingly, the convolutional nature of such a relationship implies that the reduced field can be related to the radiating component of the induced currents. A direct consequence of such a result is that the orthogonality sampling method is capable of imaging discontinuities within the unknown targets and hence identify regions with different electromagnetic properties. This possibility represents a unique feature among qualitative inverse scattering methods, as these methods have been introduced as tools to image just the morphology of the unknown targets. The new interpretation, as well as the distinctive capability of the orthogonality sampling method are proved with examples with both simulated and experimental data.**

***Index Terms*—inverse scattering problem, microwave imaging, orthogonality sampling method, shape reconstruction.**

I. Introduction

MICROWAVE imaging (MWI) has the potential to quantitatively retrieve in a non-invasive way the electromagnetic and morphological properties of unknown targets, by relying on a proper combination of scattering experiments and data processing techniques [1]. As a consequence, MWI is relevant to several applications, such as biomedical imaging [2],[3], subsurface sensing [4],[5], or through-wall imaging [6], only to mention some. However, successful application of MWI requires to deal with the non-linearity and ill-posedness of the underlying inverse scattering problem [7],[8].

Among the various approaches developed in literature [1], *qualitative* inverse scattering methods overcome the problem's non-linearity by relying on simpler, yet typically still ill-posed, problems and without requiring approximations [9]. In doing so, they turn down the possibility to retrieve the electromagnetic properties of the scatterers and only aim at recovering the support of the unknown targets.

Many different qualitative strategies have been proposed in the literature, such as multiple signal classification (MUSIC), the decomposition of time reversal operator (DORT), the linear sampling method (LSM), the factorization method (FM) and the orthogonality sampling method (OSM) [10]-[14]. Another promising and recently introduced approach is based on equivalence principles and compressive sensing [15],[16]. Typically, all these methods rely on an indicator function, whose behavior *qualitatively* provides an estimate of the target's shape. In doing so, they require solving a linear ill-posed inverse problem. As such, they need to be equipped with proper regularization strategies.

In this respect, the OSM represents a remarkable exception, as computing its indicator does not require solving an inverse problem [14] but is based on the evaluation of a *reduced* scattered field, simply defined as the scalar product between the measurements of the far-field pattern and a test function. For this reason, the OSM exhibits a significant robustness to noise, paired with an incomparable straightforwardness of implementation. Moreover, the OSM is very effective in practice, as it can be adapted to different measurement configurations, by exploiting *diversity* achieved through different combinations of incidence directions, observation directions and frequencies. Recently, the OSM has been extended to the case of near-field measurements [17], thus bridging the gap between the far-field data required in the original mathematical formulation [14] and the scattered fields actually measured in experiments.

Because of these interesting features, an understanding of the physics underlying the OSM is of course desirable, in order to take full advantage of the method, as well as comprehend its limitations. In this respect, a first interpretation recognizes the reduced scattered field as a superposition of plane waves back-propagated into the region of the scatterer [14],[17]. Additional understanding has been provided in [18], where the indicator function is related to the zeroth order Fourier coefficient of the far-field pattern of the scattered field (in a suitably translated

This is the postprint version of the following article: M. T. Bevacqua, T. Isernia, R. Palmeri, M. N. Akinci and L. Crocco, "Physical Insight Unveils New Imaging Capabilities of Orthogonality Sampling Method," in IEEE Transactions on Antennas and Propagation, 2020. doi: 10.1109/TAP.2019.2963229. Article has been published in final form at: https://ieeexplore.ieee.org/document/8951441.

0018-926X © 2020 IEEE. Personal use of this material is permitted. Permission from IEEE must be obtained for all other uses, in any current or future media, including reprinting/republishing this material for advertising or promotional purposes, creating new collective works, for resale or redistribution to servers or lists, or reuse of any copyrighted component of this work in other works.

coordinate system). However, this latter interpretation holds true only when the size of the scatterers is small with respect to the wavelength. Other considerations are given in [19] but without achieving a general physical interpretation.

In this paper, a further and deeper investigation on the physics underlying OSM is given. This latter is built on the derivation of the mathematical relationship between the reduced scattered field and the currents induced inside the investigated domain, which is reinterpreted as a convolution product. Then, the reduced scattered field is directly related to the radiating currents induced in the targets, thus explaining the capability of the method of retrieving the support of the unknown targets embedded in the domain under investigation. A second interesting consequence of the identified relation between the induced currents and the reduced field is that the OSM indicator can detect discontinuities inside the investigated objects and thus reveal regions with different electromagnetic properties. Hence, the proposed physical insight unveils the unique capability of OSM as compared to other qualitative imaging methods of providing additional information on the unknown targets besides their morphology.

The paper is organized as it follows. In Section II, the inverse scattering problem is formulated. In Section III, a brief review of the OSM is reported, while section IV introduces the physical interpretation herein proposed. Finally, in Section V some examples against simulated and experimental data are reported to demonstrate the capability of OSM of imaging discontinuities inside the investigated objects. Conclusions follow. Throughout the paper the case of scalar fields for which OSM theoretical results hold true [14],[17] is considered and a time harmonic factor $exp\{j\omega t\}$ is assumed and dropped.

II. Statement of The Problem

Let Ω denote the region under test where the targets are located. The contrast function $\chi(\boldsymbol{r}) = {\epsilon_s(\boldsymbol{r})}/{\epsilon_b} - 1$ relates the unknown properties of the scatterers to those of the host medium, being ϵ_s and ϵ_b the complex permittivities of the scatterer and the background medium, respectively and $\boldsymbol{r} \in \mathbb{R}^2$ or $\mathbb{R}^3$. The unknown targets are probed with a set of incident fields transmitted by some antennas located in $\boldsymbol{r_t} = R\,\hat{\boldsymbol{r}}_{\boldsymbol{t}}$ on a close circular curve Γ of radius R located in the far zone of the scatterers. Without any loss of generality, let us assume that the scattered fields are measured by receiving antennas at $\boldsymbol{r_m} \in \Gamma$, with $\boldsymbol{r_m} = R\,\hat{\boldsymbol{r}}_{\boldsymbol{m}}$. Under the above assumptions, the equations describing the scalar scattering problem can be expressed in the integral form as [1],[7]:

$$E_s(\hat{\boldsymbol{r}}_{\boldsymbol{m}}, \hat{\boldsymbol{r}}_{\boldsymbol{t}}) = \int_{\Omega} G_b(\hat{\boldsymbol{r}}_{\boldsymbol{m}}, \boldsymbol{r}')\,\chi(\boldsymbol{r}')E(\boldsymbol{r}', \hat{\boldsymbol{r}}_{\boldsymbol{t}})d\boldsymbol{r}' = \mathcal{A}_e[\chi E] = \mathcal{A}_e[W] \tag{1}$$

$$E(\boldsymbol{r}, \hat{\boldsymbol{r}}_{\boldsymbol{t}}) = E_i(\boldsymbol{r}, \hat{\boldsymbol{r}}_{\boldsymbol{t}}) + \int_{\Omega} G_b(\boldsymbol{r}, \boldsymbol{r}')\,\chi(\boldsymbol{r}')E(\boldsymbol{r}', \hat{\boldsymbol{r}}_{\boldsymbol{t}})d\boldsymbol{r}' = E_i + \mathcal{A}_i[\chi E] = E_i + \mathcal{A}_i[W] \tag{2}$$

where E_i, E_s and E are the incident, scattered and total field, respectively, W is the contrast source, $\boldsymbol{r} \in \Omega$. $G_b(\boldsymbol{r}, \boldsymbol{r}')$ is the Green's function pertaining to the background medium. Finally, $\mathcal{A}_e$ and $\mathcal{A}_i$ are a short notation for the integral radiation operators.

The problem (1)-(2) is non-linear, as the contrast sources W (or equivalently the total field E) also depend on the unknown of the problem, i.e. the contrast function χ. Moreover, it is also ill-posed due to the properties of the operator $\mathcal{A}_e$ [7],[8].

III. Orthogonality Sampling Method: a Brief Summary

The OSM consists in reconstructing the *reduced scattered field* from the far-field pattern ${E_s}^{\infty}(\hat{\boldsymbol{r}}_{\boldsymbol{m}}, \hat{\boldsymbol{r}}_{\boldsymbol{t}})$, defined as:

$${E_s}^{\infty}(\hat{\boldsymbol{r}}_{\boldsymbol{m}}, \hat{\boldsymbol{r}}_{\boldsymbol{t}}) = \int_{\Omega} {G_b}^{\infty}(\hat{\boldsymbol{r}}_{\boldsymbol{m}}, \boldsymbol{r}')\,\chi(\boldsymbol{r}')E(\boldsymbol{r}', \hat{\boldsymbol{r}}_{\boldsymbol{t}})d\boldsymbol{r}' \tag{3}$$

with ${G_b}^{\infty}$ denoting the Green's function in far-field zone:

$${G_b}^{\infty}(\hat{\boldsymbol{r}}_{\boldsymbol{m}}, \boldsymbol{r}) = \gamma e^{-jk_b \boldsymbol{r}\cdot\hat{\boldsymbol{r}}_m} \tag{4}$$

wherein $k_b = \omega\sqrt{\mu_b \varepsilon_b}$ is the wavenumber in the host medium and γ is a constant for a fixed frequency [14],[17]. Then, the reduced scattered field is defined as [14]:

$${E_s}^{red}(\boldsymbol{r}, \hat{\boldsymbol{r}}_{\boldsymbol{t}}) = \int_{\Gamma} {E_s}^{\infty}(\hat{\boldsymbol{r}}_{\boldsymbol{m}}, \hat{\boldsymbol{r}}_{\boldsymbol{t}})\, e^{jk_b \boldsymbol{r}\cdot\hat{\boldsymbol{r}}_m}\, d\hat{\boldsymbol{r}}_{\boldsymbol{m}} = \frac{1}{\gamma}\langle {E_s}^{\infty}, {G_b}^{\infty}\rangle_{\Gamma} \tag{5}$$

where $\langle\cdot,\cdot\rangle$ denotes the scalar product. Equation (5) simply represents the scalar product over the measurement domain Γ of the measured far field pattern with the test function $e^{-jk\boldsymbol{r}\cdot\hat{\boldsymbol{r}}_m}$. As such, the equation tests the *orthogonality* relation between the far-field pattern and the Green function in far zone (apart from the constant γ).

The OSM indicator function $I(\boldsymbol{r})$ is defined as [14]:

$$I(\boldsymbol{r}) = \int_{\Gamma} \left|{E_s}^{red}(\boldsymbol{r}, \hat{\boldsymbol{r}}_{\boldsymbol{t}})\right|^2 d\,\hat{\boldsymbol{r}}_{\boldsymbol{t}} = \left\|{E_s}^{red}(\boldsymbol{r}, \hat{\boldsymbol{r}}_{\boldsymbol{t}})\right\|_{\Gamma}^{\boldsymbol{2}} \tag{6}$$

where $\|\cdot\|_{\Gamma}^2$ is the l_2-norm on Γ. By construction, the indicator $I(\boldsymbol{r})$ achieves large values when the far-field pattern approaches the one of the background Green's function for the considered sampling point. In particular, larger values are assumed in sampling points belonging to the support of the targets [14]. As a consequence, by selecting a fixed threshold, the indicator function allows to discriminate between points inside and outside the targets, thus characterizing their shape.

It is worth noting that, opposite to other qualitative methods, the OSM does not involve the solution of any ill-posed inverse problem, since its indicator (6) is directly obtained from the evaluation of the scalar product (5) in each sampling point of the imaged region.

As a further feature, it is important to recall that unlike the

LSM or the FM which only work with multiview-multistatic data, the OSM exhibits some flexibility with respect to data to be processed. For instance, in equations (5) and (6), multiview data at a single frequency are considered. However, multifrequency measurements for a single-view can be exploited by simply replacing the integration with respect to incidence directions with the one on the available frequencies. Of course, the use of both multifrequency and multiview data is also possible. In this case, the indicator is defined as it follows:

$$I_{MF}(\boldsymbol{r}) = \int_B \int_\Gamma \left| {E_s}^{red}(\boldsymbol{r}, \hat{\boldsymbol{r}}_t, \omega) \right|^2 d\,\boldsymbol{r}_t\, d\omega \tag{7}$$

where the angular frequency $\omega \in B$ and B is the relevant frequency band.

IV. Physical Interpretation of OSM

In order to get a better physical understanding of the method, it proves useful to exploit an alternative expression of the reduced scattered field. To this end, following [14], one can substitute into (5) the explicit relation (3) between the far-field pattern and the induced currents. By inverting the integration order, equation (5) can be rewritten as:

$${E_s}^{red}(\boldsymbol{r}, \hat{\boldsymbol{r}}_t) = \int_\Omega W(\boldsymbol{r}', \hat{\boldsymbol{r}}_t) d\boldsymbol{r}' \int_\Gamma \gamma e^{-jk_b(\boldsymbol{r}'-\boldsymbol{r})\cdot\hat{\boldsymbol{r}}_m}\, d\hat{\boldsymbol{r}}_m \tag{8}$$

Then, by taking advantage from the Funck-Hecke formula [9] (which is valid as long as Γ is a closed curve), the reduced scattered field, at a fixed frequency and for a fixed illumination condition, can be rewritten as [14],[17]:

$${E_s}^{red}(\boldsymbol{r}) = \begin{cases} \int_\Omega \gamma \alpha_0\, J_0(k_b|\boldsymbol{r}-\boldsymbol{r}'|)\, W(\boldsymbol{r}')\, d\boldsymbol{r}', \boldsymbol{r} \in \mathbb{R}^2 \\ \int_\Omega \gamma \alpha_0\, j_0(k_b|\boldsymbol{r}-\boldsymbol{r}'|)\, W(\boldsymbol{r}')\, d\boldsymbol{r}', \boldsymbol{r} \in \mathbb{R}^3 \end{cases} \tag{9}$$

where α_0 is a constant related to the Funck-Hecke formula, (which is equal to 2π and 4π in 2D and 3D geometry[1], respectively), and J_0 and j_0 stand for the Bessel function of zeroth order and spherical Bessel function of zeroth order, respectively.

By the sake of simplicity and taking into account that the induced currents have the same support of the targets (so that the actual contrast sources assume zero values outside it), let us extend the integrals (9) to $\mathbb{R}^2$ and $\mathbb{R}^3$, respectively. By so doing, the left-hand side can be interpreted as the convolution product between the contrast source W and the relevant zero order Bessel function, (which also represents the non-singular part of the Green function, see [7]). Accordingly, the alternative expression of the reduced scattered field can be cast in a compact way as it follows:

$${E_s}^{red}(\boldsymbol{r}) \propto \begin{cases} J_0(k_b|\boldsymbol{r}|) * W(\boldsymbol{r}) = \mathcal{F}^{-1}\{\mathcal{F}\{J_0\}\,\mathcal{F}\{W\}\}, \boldsymbol{r} \in \mathbb{R}^2 \\ j_0(k_b|\boldsymbol{r}|) * W(\boldsymbol{r}) = \mathcal{F}^{-1}\{\mathcal{F}\{j_0\}\,\mathcal{F}\{W\}\}, \boldsymbol{r} \in \mathbb{R}^3 \end{cases} \tag{10}$$

wherein the symbol $*$ indicates the convolutional product, while $\mathcal{F}$ and $\mathcal{F}^{-1}$ represents the Fourier transform and its inverse, respectively. Thanks to this convenient rewriting of the equation (5), the reduced scattered field can be seen as the output of a linear system whose impulsive response is given (apart from a constant) by the Bessel functions, and whose input are the contrast sources. As a consequence, in the spectral domain the reduced scattered field is the product between the Fourier transform of W and the one of the Bessel function at hand. Then, by taking advantage from the Fourier transform of the Bessel functions (which is given by a single layer distribution along the circle (sphere) $k = k_b$ [20],[21]), the Fourier Transform of the reduced scattered field can be finally read (but for a constant) as the restriction to the circle (or sphere) of radius k_b of the Fourier transform of the contrast sources.

Such a circumstance has two interesting consequences.

First, the presence of the Bessel function in the integral entails the selection of the spectral components of the currents located on a circle (sphere) of radius k_b. This is a very interesting result in view of the fact, discussed in detail in [22],[23], that the radiating sources exactly oscillate at the frequency k_b. Hence, the reduced scattered field ${E_s}^{red}$ can be related to the radiating sources induced by a given illumination[2].

Then, as the actual contrast sources have the same support as the targets, and the reduced scattered field is a kind of subset of these latter, one has a simple understanding of why the OSM indicator permits to retrieve their support. In fact, in (6) and (7) one is plotting the superposition of the square amplitude of the contrast sources at hand.

An interesting consequence of both equations (9) is that the reduced scattered field, being related to the currents and, hence, to the contrast function, is expected to exhibit a distribution which depends on the electromagnetic properties of the investigated objects. In fact, since the scalar fields at hand are continuous at discontinuities, the OSM indicator will be characterized by larger values in those points corresponding to electrically denser regions inside the target, thus allowing to identify the presence of discontinuities within the retrieved support. This relevant feature will be discussed and validated in the numerical Section, where some exemplification of the physical meaning of the reduced field is also given.

Finally, it is important to underline that the herein proposed physical interpretation holds true for near field [17] and aspect limited [19],[24] measurement configurations, as in both cases truncation effects in the spatial domain come into play.

[1] The 3D scalar problem is considered.

[2] Notably, the results in [22],[23] still do not imply that the Fourier transform of the radiating currents are located just on the circle (sphere) of radius k_b, as

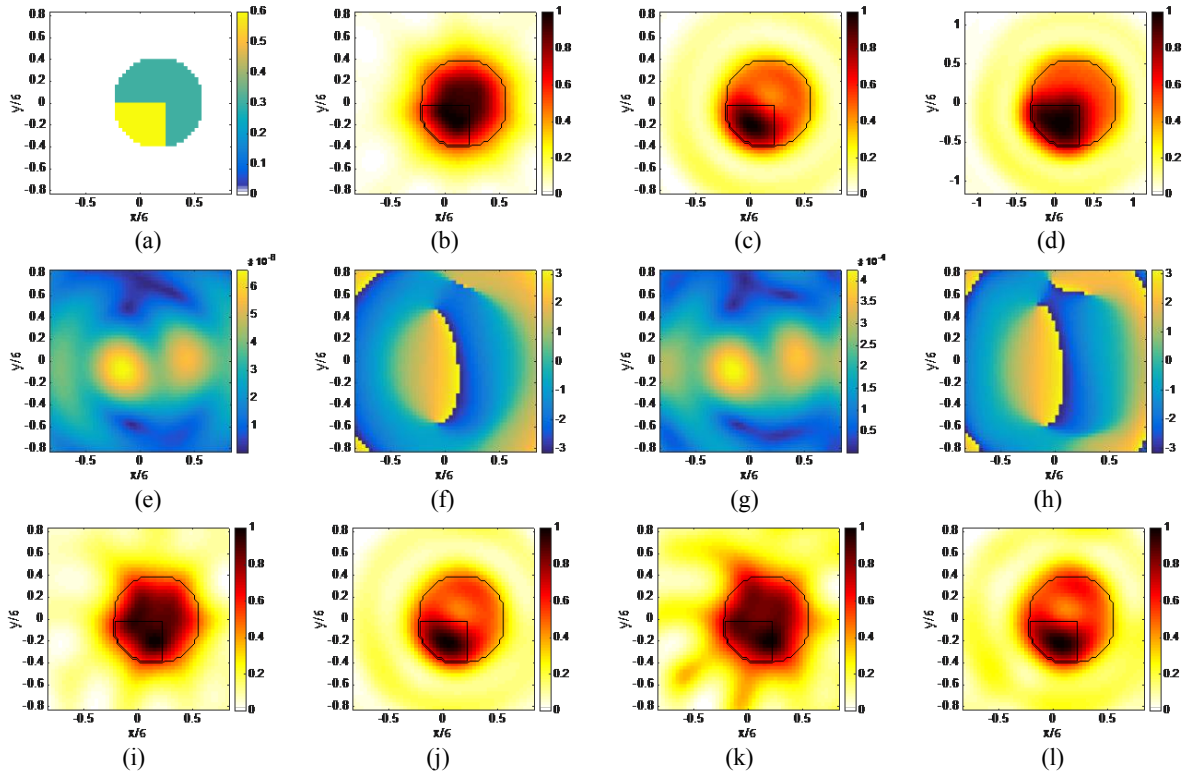

Figure 1. Assessing the physical interpretation of OSM on simulated data. (a) Real part of the reference contrast. Normalized (b) LSM, (c) OSM and (d) multifrequency OSM indicators. Amplitudes and phases of (e)-(f) the reduced scattered field and (g)-(h) reconstructed radiating currents. (i)-(j) as (b)-(c) but for SNR=10 dB. (k)-(l) as (b)-(c) but for SNR=3 dB.

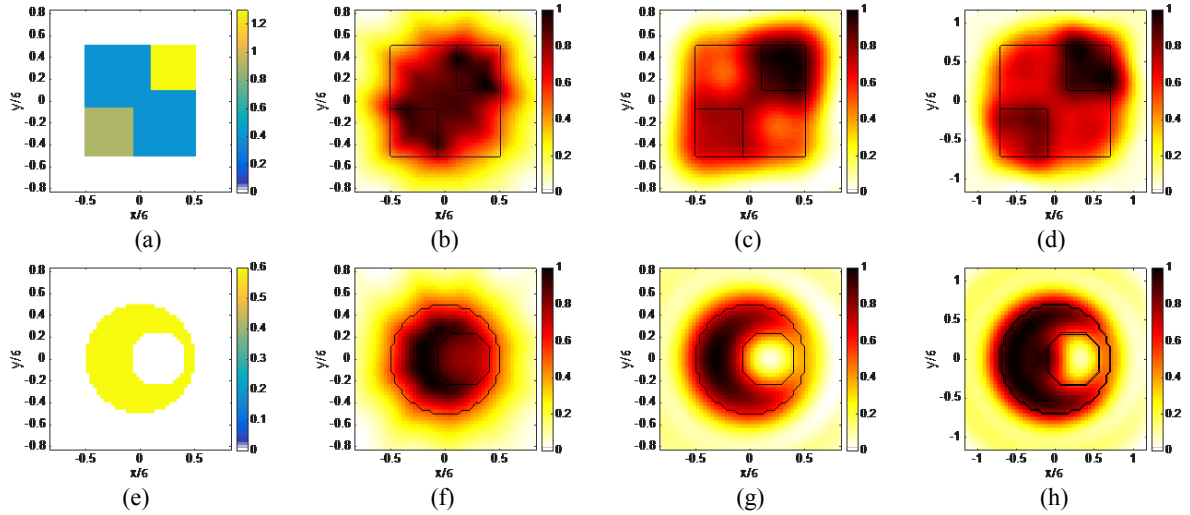

Figure 2. Assessing the OSM capability of identifying regions with different electric properties: (a)-(e) Reference contrast functions. Normalized (b)-(f) LSM, (c)-(g) OSM and (d)-(h) multifrequency OSM indicators.

the corresponding reduced scattered field (see [17],[19],[24] for more details) is related to the induced currents by means of the linear relationship in eq. (9).

V. Numerical Validation

In this section a controlled assessment with simulated data is firstly carried out. Then, the OSM performance are evaluated

against the experimental data-set provided by the Institute Fresnel of Marseille [25],[26], typically adopted to benchmark inverse scattering procedures. In the following, we consider the canonical 2D scalar problem (TM polarized fields).

A. Simulated data

In these examples, one or more unknown objects have been positioned inside a square domain of side L and, following [27], the same number of receivers and transmitters $\mathrm{N} = \mathrm{M}$, modelled as line sources located on a circumference Γ of radius R, has been considered. The scattered field data, simulated by means of a full-wave forward solver based on the method of moments, have been corrupted with a random Gaussian noise with a given SNR. A working frequency of 5GHz has been considered. In the multifrequency case, the adopted frequency range is 4-7GHz with a step of 0.25GHz.

The results have been compared with those obtained with the LSM. In particular, in order to perform a fair comparison, both indicators have been normalized. In particular, the OSM indicator (6) has been normalized to its maximum value, while the LSM indicator has been rescaled as described in [28]. Note that in (6) we focus on l_2-norm but similar results can be obtained by adopting the l_1-norm.

The first example deals with a lossless and inhomogeneous circular cylinder embedded in the air, see figure 1.(a), with $\mathrm{L} = 1.67\ \lambda$. Following [29], a number of cells N_c equal to 50×50 has been used (with size $0.034\ \lambda$), while $\mathrm{N} = \mathrm{M} = 16$, $\mathrm{SNR} = 30\mathrm{dB}$ and $\mathrm{R} = 3.33\ \lambda$. In order to validate the proposed physical interpretation, the reduced scattered field defined in equation (5) has been compared with the reconstructed radiating currents obtained from (1) via Tikhonov regularization [8]. The amplitudes and phases of the reduced scattered field and the thus obtained currents for a single transmitter position $\hat{\boldsymbol{r}}_{\boldsymbol{t}}$ are shown in figures 1.(e)-(h).

Figures 1.(b)-(d) depict the normalized LSM, OSM and multifrequency OSM indicators, respectively. As it can be seen, in both cases the position and shape of the unknown cylinder has been correctly retrieved, especially in case of multifrequency data processing. Moreover, unlike LSM, the OSM indicator assumes higher values, i.e., closer to 1, in the denser part of the targets and lower values in the remainder part of the support, thus allowing to identify the discontinuity which is present in the unknown profile. A further analysis has been performed by changing the SNR, thus confirming the robustness of the OSM with respect to the measurement errors (see figures 1.(i)-(l)).

The interesting capability of OSM to identify the inner discontinuities encourages us to further investigate its performance by considering other inhomogeneous profiles. In particular, with respect to the same imaging domain and measurement setup as in the first example, a non-homogeneous square target and a ring scatterer have been considered (see figure 2). As it can be seen, both LSM and OSM correctly retrieve the support of the two targets. However, the OSM indicator allows to detect the presence of a denser region inside the square target and the hole inside the non-convex target, respectively. As such, OSM can retrieve the support of unknown targets also in case of not simply connected objects. Conversely, the LSM maps does not allow to identify discontinuities or holes inside the scatterers.

B. Experimental data

In this subsection, we have considered three dataset in the Fresnel database, namely:

- *FoamDielIntTM*, which is a piecewise inhomogeneous dielectric target made by two nested, non-concentric, circular cylinders, where the inner one has a higher contrast ($\epsilon_s = 3 \pm 0.3$) than the outer one ($\epsilon_s = 1.45$) [26];
- *FoamTwinDielIntTM*, in which another circular cylinder ($\varepsilon = 3 \pm 0.3$) is placed in contact with the *FoamDielIntTM* target [26].
- *U-TM shaped*, which is a metallic U-shaped target with dimension 80×50 mm2[25].

The data are collected under a partially aspect limited configuration, where primary sources completely surround the targets, but, for each illumination, the measurements are taken only on an angular sector of 240°, that is, excluding a 120° sector centered on the incidence direction. The complete description of the targets and the measurement set-up can be found in [25],[26].

The investigated area of 0.2 x 0.2m2 has been discretized in 78×78 cells. For the *FoamTwinDielIntTM* target, the working frequency has been selected equal to 4GHz, while a 36×18 multiview-multistatic data matrix has been considered. On the contrary, for the *FoamDielIntTM* target, a 45×36 multiview-multistatic data matrix at 5GHz has been processed. Finally, for the last target, the results have been obtained by processing at 12GHz a 72×36 data matrix

The indicators are shown in figure 3. In particular, figures 3(a)-(f) again confirm that OSM allows to clearly discriminate the presence of inhomogeneities inside the targets. In particular, the OSM indicator can be quantized in three different levels pertaining to the different electrical properties (of course, the value of these properties cannot be guessed from it).

The results of the last example, reported in figures 3(g)-(i), confirm that OSM succeeds also in imaging non-convex targets, as already observed in the previous subsection (see figures 2(e)-(h)). Note that OSM indicator is also reliable in case of metallic targets, which are characterized by induced currents only localized in proximity of the boundary of the targets.

VI. Conclusions

Among qualitative methods, the OSM has recently gained increasing interest in inverse scattering literature, thanks to its simplicity and flexibility. However, despite these interesting properties, a full understanding of the physics underlying the method has been not yet given.

In this paper, an original physical interpretation of the OSM has been introduced, by properly handling the reduced scattered field formulation. In particular, the reduced scattered field has been related to the radiating part of the induced currents. This may suggest that a more proper terminology would be to refer to it as *reduced contrast source*.

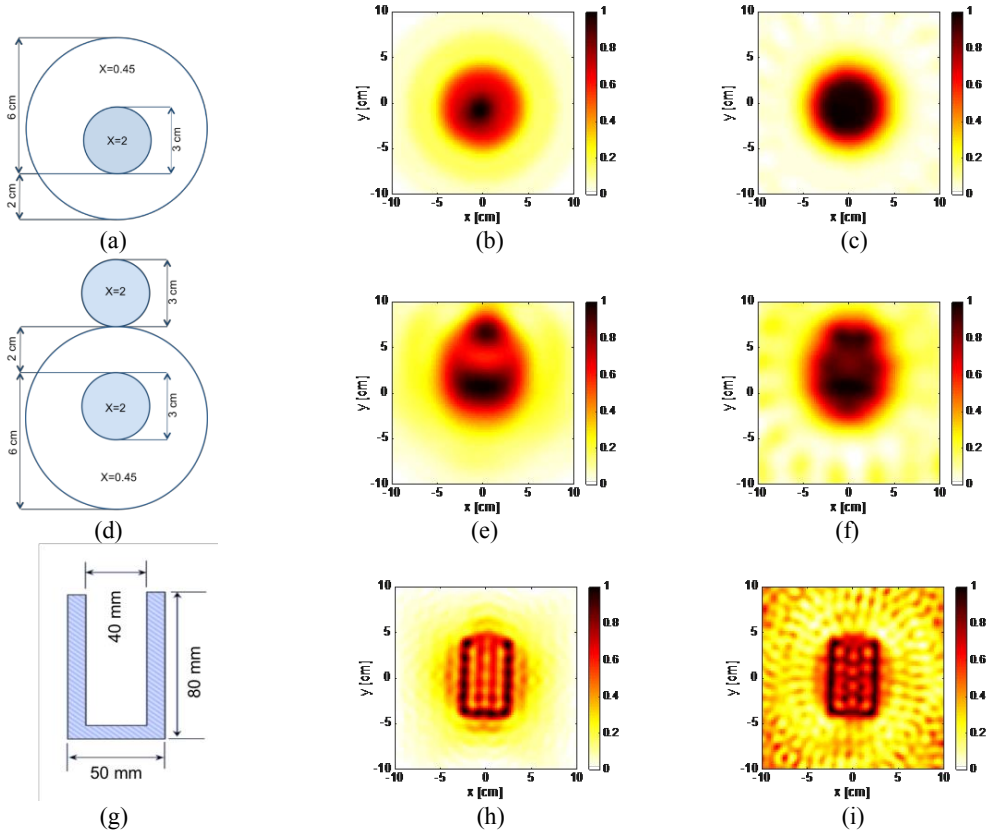

Figure 3. Results with benchmark experimental data. Sketch of the reference profiles: (a) *FoamDielIntTM*, (d) *FoamTwinDielIntTM* and (g) *U-TM shaped*. Normalized (b)-(e)-(h) OSM and (c)-(f)-(i) LSM indicators. The size of the discretization cells is about 0.07 λ, 0.03 λ and 0.10 λ, respectively.

Besides lexicon, the proposed physical interpretation allows to immediately understand why the OSM indicator is capable of identifying the support of the unknown targets, since contrast sources and scatterers share the same support. Furthermore, it allows to foresee the expected limitations of OSM, which will be related to the presence of a significant non-radiating component of the contrast sources. Indeed, this component will leave no trace into the measured data which are used to build the indicator function.

Finally, as the induced currents have not only the same support as the scatterers, but also the same internal discontinuities, the proposed interpretation has allowed us to show that the OSM indicator is able to identify regions within the unknown targets where abrupt changes in electromagnetic properties occur. This interesting circumstance represents a unique feature in the framework of qualitative methods, as confirmed here by the compared application of the OSM and the LSM to simulated and experimental benchmark data. In these examples, the OSM has also exhibited an improved capability of identifying the support of non-convex targets.

The good performance observed as well as the relevant physical meaning herein proposed, makes the OSM and the reduced scattered field (or the *reduced contrast source*) mostly attractive in quantitative imaging. Indeed, any information about radiative components of the currents [30],[31] and the inner structure of the region under test [32],[33] can play a key role in quantitatively determining the electromagnetic properties of the targets, or even build new approximate inversion. To this end, future work will be devoted at exploiting the proposed physical interpretation and information about discontinuities to retrieve not only the morphology of the targets but also their electromagnetic properties, as well as to exploit the OSM in the so-called virtual experiments framework [28],[34].

REFERENCES

[1] M. Pastorino, Microwave Imaging, John Wiley & Sons, Hoboken, N J, 2010.

[2] R. C. Conceição, J. J. Mohr, and M. O'Halloran, (Eds.), *An Introduction to Microwave Imaging for Breast Cancer Detection*, 1st ed., Biological and Medical Physics, Biomedical Engineering, Switzerland: Springer International Publishing, 2016.

[3] L. Crocco, R. C. Conceição, M. L. James, I. Karanasiou, (Eds.), *Emerging Electromagnetic Technologies for Brain Diseases Diagnostics, Monitoring and Therapy*, Springer, Cham, 2018.

[4] A. S. Turk, A. K. Hocaoglu, A. A. Vertiy (Eds.), *Subsurface Sensing*, Wiley, 2011.

[5] R. Persico. *Introduction to Ground Penetrating Radar: Inverse Scattering and Data Processing*, Wiley, 2014.

[6] M. Amin (Ed) *Through-the-wall radar imaging*, CRC Press 2010.

[7] D. Colton and R. Kress, "Inverse Acoustic and Electromagnetic Scattering Theory", *Springer-Verlag,* Berlin, Germany, 1998.

[8] M. Bertero and P. Boccacci, "Introduction to Inverse Problems in Imaging", *Institute of Physics*, Bristol, UK, 1998.

[9] F. Cakoni and D. Colton, *Qualitative methods in inverse scattering Theory*, Springer-Verlag, Berlin, Germany, 2006.

[10] H. Ammari, E. Iakovleva, D. Lesselier, G Perrusson, "MUSIC-type electromagnetic imaging of a collection of small three-dimensional inclusions", *SIAM Journal on Scientific Computing*, vol 29 n. 2, pp. 674-709, 2007.

[11] H. Tortel, G. Micolau, and M. Saillard, "Decomposition of the time reversal operator for electromagnetic scattering", *J. Electromagn. Waves Appl.*, vol. 13, n. 5, pp. 687-719, 1999.

[12] D. Colton, H. Haddar, and M. Piana, "The linear sampling method in inverse electromagnetic scattering theory", *Inverse Probl.*, 19: 105–137, 2003.

[13] A. Kirsch, N. I. Grinberg, "The Factorization Method for Inverse Problems", *Cambridge*, 2008.

[14] R. Potthast, "A study on orthogonality sampling", *Inverse Prob*., vol. 26, n. 7, 2010.

[15] M. Bevacqua and T. Isernia, "Shape reconstruction via equivalence principles, constrained inverse source problems and sparsity promotion," *Progress In Electromagnetics Research*, vol. 158, 37-48, 2017.

[16] M. T. Bevacqua and T. Isernia, "Boundary Indicator for Aspect Limited Sensing of Hidden Dielectric Objects," *in IEEE Geoscience and Remote Sensing Letters*, vol. 15, no. 6, pp. 838-842, June 2018.

[17] M. N. Akıncı, M. Çayören ve I. Akduman, "Near-Field Orthogonality Sampling Method for Microwave Imaging: Theory and Experimental Verification", *IEEE Trans. Microw. Theory Techn*., vol. 64, n.8, pp. 2489-2501, Aug. 2016.

[18] R.Griesmaier, "Multi-frequency orthogonality sampling for inverse obstacle scattering problems", *Inverse Probl.*, vol. 27, 2011.

[19] M. N. Akıncı, "Improving Near-Field Orthogonality Sampling Method for Qualitative Microwave Imaging," in *IEEE Transactions on Antennas and Propagation*, vol. 66, no. 10, pp. 5475-5484, Oct. 2018.

[20] R. Piessens, "The Hankel Transform," The Transforms and Applications Handbook, §9, Alexander D. Poularikas, Boca Raton: CRC Press LLC, 2000.

[21] G. S. Adkins, "Three-dimensional Fourier transforms, integrals of spherical Bessel functions, and novel delta function identities", *Bull. Allahabad Math. Soc,* vol. 31, pp. 215-246, 2016.

[22] A. J. Devaney, and E. Wolf, "Radiating and Nonradiating Classical Current Distributions and the Fields They Generate", *Phys. Rev. D*, vol. 8, n.4, 1973.

[23] E. A. Marengo and R. W. Ziolkowski, "Nonradiating and minimum energy sources and their fields: generalized source inversion theory and applications," in *IEEE Transactions on Antennas and Propagation*, vol. 48, no. 10, pp. 1553-1562, Oct. 2000.

[24] M. Nuri Akinci, "An Efficient Sampling Method for Cross-Borehole GPR Imaging," in *IEEE Geoscience and Remote Sensing Letters*, vol. 15, no. 12, pp. 1857-1861, Dec. 2018.

[25] K. Belkebir and M. Saillard, "Special section: Testing inversion algorithms against experimental data", *Inverse Probl.*, 17:1565–2028, 2001.

[26] K. Belkebir and M. Saillard, "Special section: Testing inversion algorithms against real data: Inhomogeneous targets", *Inverse Probl.*, 21, 2005

[27] O. M. Bucci and Isernia T., "Electromagnetic inverse scattering: Retrievable nformation and measurement strategies", *Radio Sci*., 32: 2123–2138, 1997.

[28] L. Di Donato, M. T. Bevacqua, L. Crocco and T. Isernia, "Inverse Scattering Via Virtual Experiments and Contrast Source Regularization," *IEEE Trans. Antennas Propag.*, vol. 63, no. 4, pp. 1669-1677, April 2015.

[29] J. Richmond, "Scattering by a dielectric cylinder of arbitrary cross section shape," *IEEE Trans. Antennas Propag*., vol. 13, no. 3, pp. 334-341, 1965.

[30] X. Ye and X. Chen, "Subspace-Based Distorted-Born Iterative Method for Solving Inverse Scattering Problems," *IEEE Trans. Antennas Propagat*, vol. 65, no. 12, pp. 7224-7232, Dec. 2017.

[31] X. Chen, "Subspace-Based Optimization Method for Solving Inverse-Scattering Problems," I*EEE Trans. on Geoscience and Remote Sensing*, vol. 48, no. 1, pp. 42-49, Jan. 2010.

[32] A. Rahimov, A. Litman and G. Ferrand, "MRI-based electric properties tomography with a quasi-Newton approach," *Inverse Problems,* vol. 33, 105004, 2017.

[33] M. Bevacqua, G. Bellizzi, T. Isernia, L. Crocco, "A Method for Effective Permittivity and Conductivity Mapping of Biological Scenarios via Segmented Contrast Source Inversion", *Progress In Electromagnetics Research*, Vol. 164, pp. 1-15, 2019.

[34] L. Di Donato, M. Bevacqua, T. Isernia, I. Catapano, L. Crocco, "Improved quantitative microwave tomography by exploiting the physical meaning of the Linear Sampling Method," *Proceedings of the 5th European Conference on Antennas and Propagation (EUCAP),* vol., no., pp.3828-3831, 11-15 April 2011.